Wind effect in turbulence parametrization

M. Colombini *, A. Stocchino

Dipartimento di Ingegneria Ambientale, Università di Genova, Italy

Abstract

The action of wind blowing over a closed basin ultimately results in a steady shear-induced circulation pattern and in a leeward rising of the free surface—and a corresponding windward lowering—known as wind set-up. If the horizontal dimensions of the basin are large with respect to the average flow depth, the occurrence of local quasi-equilibrium conditions can be expected, i.e. the flow can be assumed to be locally driven only by the wind stress and by the opposing free surface gradient due to set-up. This wind-induced flow configuration shows a strong similarity with turbulent Couette–Poiseuille flow, the one dimensional flow between parallel plates generated by the simultaneous action of a constant pressure gradient and of the shear induced by the relative motion of the plates. A two-equation turbulence closure is then employed to perform a numerical study of turbulent Couette–Poiseuille flows for different values of the ratio of the shear stresses at the two walls. The resulting eddy viscosity vertical distributions are analyzed in order to devise analytical profiles of eddy viscosity that account for the effect of wind. The results of this study, beside allowing for a physical insight on the turbulence process of this class of flows, will allow for a more accurate description of the wind effect to be included in the formulation of quasi-3D and 3D models of lagoon hydrodynamics.
© 2005 Elsevier Ltd. All rights reserved.

Keywords: Wind-driven flow; Couette–Poiseuille flows; Eddy viscosity; Shallow water; Two-equation turbulence closure

1. Introduction

Water quality modelling in natural or artificial water bodies like lakes, reservoir, estuaries and coastal zone requires the prior knowledge of the circulation flow. The transport of a passive or active pollutant can be described with sufficient accuracy if the hydrodynamics is known. The simulation of more complex phenomena, like sediment transport, involves the evaluation of the shear stress acting on the bed, which in turn is able to modify the shape of the domain in which the flow itself evolves.

Mathematical models based on the shallow-water approximation have quite a long tradition for the solu-

tion of this class of flows, due to the sharp separation between the vertical and the horizontal spatial scales that allows for solving the problem in terms of the depth-averaged horizontal velocity components, disregarding the role of the vertical velocity.

However, the knowledge of the vertical velocity and, more important, of the vertical profiles of the horizontal velocities has soon become a pressing need for the study of some practical engineering problems, like the oil-spill movement or the transport of a passive contaminant or the suspended sediment dynamics, which strongly depend on the vertical structure of the flow. Apparently the only answer to these problem is the solution of the full set of the 3D Reynolds equation, a task that however, even nowadays, can be prohibitive in terms of computer time.

In an attempt to reconcile the requirement of a more detailed solution with the slenderness and robustness of 2D models, a new generation of numerical models,

---

* Corresponding author. Address: DIAM, Via Montallegro 1, 16145 Genova, Italy. Fax: +39 10353 2478.
 E-mail addresses: col@diam.unige.it (M. Colombini), jorma@diam.unige.it (A. Stocchino).

which can be identified as a whole as quasi-3D (Q3D), appeared in the late 80s [10,23a]. These models are characterized by a primary module solving the 2D shallow water equation coupled to a secondary module that is fed with the local values of the averaged horizontal velocities and flow depth and, through the identification of a suitable vertical structure of the flow, allows for the determination of some quantities (namely the bed shear stress), which are then fed back to the main module [8]. In a way, even standard 2D models can be thought as Q3D models, since the usual choice of modelling the bed shear stress as proportional to the square of the depth-average velocity through a friction Chezy coefficient is consistent with the assumption of a vertical logarithmic profile of the velocity and of a parabolic vertical structure of the eddy viscosity.

A realistic 3D flow can thus be obtained at a much less computational cost with respect to conventional 3D models. Of course, simplifying assumptions have to be made about the vertical structure of the flow, but the two dimensional imprint of this class of flows is retained. Moreover, a rigorous derivation of the shallow water equations shows that, in the process of averaging the 3D Reynolds equations, new "stresses" appear that require a suitable closure hypothesis to be modelled. In fact, similarly to the appearance of Reynolds stresses in the averaging of Navier–Stokes equation, the nonlinearity of the advective terms produces the so-called "dispersive stresses" that are related to the vertical nonuniformity of the horizontal velocities. Dispersive stresses, together with the depth-averaged values of the Reynolds stresses acting on vertical planes, are usually disregarded in conventional 2D models, or, at most, they are modelled as a whole introducing a diffusive 'viscous' term. However, the presence of such a term is justified more on the ground of numerical instability control than on a physical basis. The a priori knowledge of the vertical profiles of velocity and eddy viscosity allows for a rigorous derivation of all the unknown stresses in the shallow water equations [5].

Many Q3D models have been formulated for the case of wind-driven circulation flow. Wind and tide are the main causes of circulation flow in small basins but while 2D models proved successful in the modelling of tide-generated flow, the numerical predictions of wind-induced circulation pattern and of the so-called set-up were not as satisfactory [15].

The success of standard 2D models in modelling tide-generated flow can be ascribed to the fact that in this case a condition of local equilibrium holds such that the logarithmic vertical profile of the horizontal velocities can be confused with its depth-averaged value and the bed shear stress quadratically depends on the depth-averaged velocity through a friction coefficient. The actual occurrence of this local equilibrium is ensured by the slow variation of all the quantities (and in particular of the free surface slope) in the horizontal directions when scaled with the local flow depth.

However, both theoretical analyses and field or laboratory measurements show that the way velocity profiles develop for the case of tidal and wind-induced circulation is remarkably different. In particular, flow reversal can be often detected along the vertical in the latter. If this is the case, the displacement of the local velocity with respect to its depth-averaged value can be large and dispersive stresses cannot be assumed to be negligible. Moreover, the quadratic dependence of the bed shear stress from the depth-averaged velocity through a friction coefficient, widely adopted in the simulation of shallow flows in the absence of wind, cannot be simply generalized to wind-driven flows.

Purpose of the present paper is to investigate the vertical structure of wind-driven flows and in particular to propose a new analytical relationship for the vertical profile of the eddy viscosity aiming at the formulation of a new quasi-3D model for flow generated by both wind and tide. As for the case of tide-generated flow, local equilibrium condition are sought and analyzed in terms of self-similar vertical profiles of eddy viscosity and velocity.

The next section is therefore devoted to the analysis of local equilibrium condition and of the analogy between these equilibrium profiles and flows of the Couette–Poiseuille (C–P) family. Then, in Section 3 the problem of turbulent C–P flow is formulated and the turbulent closure model adopted is presented. A comparison of the numerical results with the experimental data on C–P flows of El Telbany and Reynolds [4] is attempted in the following section, showing that the numerical model perform well for this flow configuration. Then, in Section 5 a discussion of the results in terms of eddy viscosity profiles is presented, together with some proposals for an analytical interpretation of the numerical results.

2. The Couette–Poiseuille flow analogy

In our search of self-similar profiles we focus on unidimensional wind-driven flows slowly varying in the longitudinal direction. A typical example is the so-called countercurrent flow, the kind of flow that shows up in a long and narrow (with respect to flow depth) closed channel where a constant wind is blown in the longitudinal direction.

This simple flow reproduces many features of 2D wind-driven flows, namely the formation of a set-up of the free surface in the wind direction, and it has been therefore widely studied both experimentally [2,7,20] and theoretically [10,19,23a,23b].

Nevertheless, for the purpose of identifying self-similar configurations, the countercurrent flow can be an

oversimplified example. In fact, continuity forces zero-mean velocities along the whole channel, a situation that locally occurs in the more general case of 2D wind-induced flow, but is undoubtly a very peculiar one. Care must then be used when extending results, namely the eddy viscosity vertical distribution, obtained from the analysis of zero-mean countercurrent flow to situation in which the depth-averaged value of velocity is not zero.

In a depth-varying cross-section, vertical profiles of velocities are quite different moving along the transverse direction. Fig. 1 shows the free surface elevation and the depth-averaged flow pattern, while Fig. 2 depicts the vertical pattern of the longitudinal velocity, reconstructed from Wu and Tsanis' Q3D solution [23a] in a closed basin with trapezoidal cross-section. In the shallow regions close to the lateral banks flow velocity is always positive (i.e. in the wind direction), while a reverse
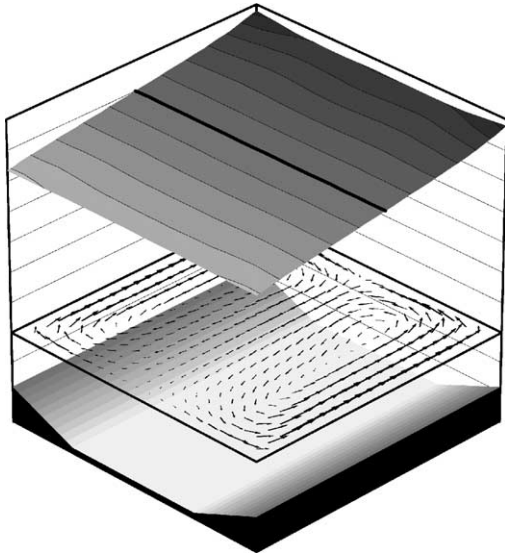

Fig. 1. Wind set-up and depth-averaged circulation pattern in a square basin of trapezoidal cross-section. Wind is blowing from left bottom to right top.
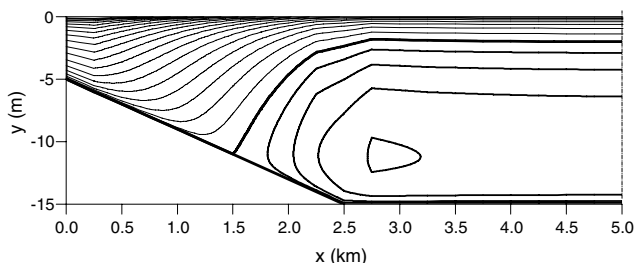

Fig. 2. Counter plot of the cross-sectional pattern of the downwind component of velocity in the basin of Fig. 1, reconstructed from [23a]. Thinner and thicker isolines represent positive (leeward) and negative (windward) values of the velocity respectively.

flow occurs in the central region. Zero-mean flow only appears at two symmetrical locations in the cross-section, corresponding to the center of the two counter-rotating cells of the depth-averaged circulation pattern.

Since the presence (or the absence) of flow reversal strongly affect the eddy viscosity distribution [8], a more general example than that of countercurrent flow has to be considered.

A condition that can be safely assumed to be valid in any region of the basin, with the only exception of the area close to the leeward and windward banks where the flow is strongly three-dimensional, is that of a linear distribution of the shear stress along the vertical. The shear stress can be thought as due to the superposition of two contributions, a constant one due to the wind stress acting on the free surface and a linear one due to the bed shear stress, which can be related to the free surface slope (the wind set-up). In this case the following equation is valid:

$$\frac{1}{\rho}\frac{\partial \tau}{\partial y} = -g\frac{\partial h}{\partial x} \tag{1}$$

where ρ is fluid density, g the gravitational acceleration, τ the shear stress, h the free surface elevation, x and y the longitudinal and vertical coordinates respectively.

Since the set-up is fairly constant along the transverse coordinate, so does the vertical gradient of the shear stress. Then, as sketched in Fig. 3, the vertical distribution of shear stress is always positive (no reversal) in the region close to the lateral banks (a), while a negative value of the bed shear stress (associated to flow reversal) is expected in the central region (c). The peculiar situation of zero bed shear stress (b) marks the boundary between the two regions. Finally, note that a typical distribution of the shear stress for the case of absence of wind is obtained by reversing the profile of Fig. 3(b).

We are now going to cast an analogy between wind-induced flow and the uniform flow between parallel plates generated by the simultaneous actions of a constant longitudinal pressure gradient and of the relative motion of one plate with respect to the other. The latter, usually referred to as flow of the Couette–Poiseuille (C–P) family, presents a strong similarity with the flow under examination.

We assume that along each vertical, flow is uniquely determined by the local values of the depth-averaged velocity U, of the depth D and of the wind stress ρu_{*s}^2, where u_{*s} is the friction velocity at the free surface. Furthermore, we stipulate that the vertical structure of the flow and of the turbulence characteristics are the same that occur in the confined case, when the distance between the plates is equal to the flow depth D, the stress transferred by the moving plate is ρu_{*s}^2 and the flow rate for unit width is UD.

In the following, turbulent C–P flows are investigated. The shear stress at the moving plate, representing
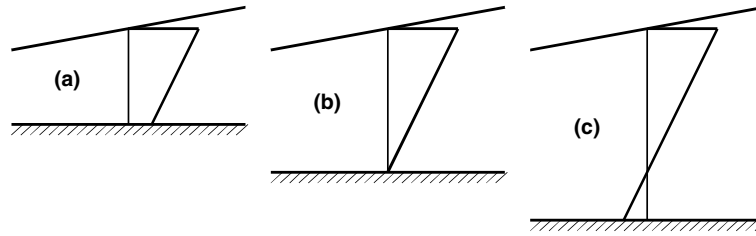
Fig. 3. Schematic of vertical shear stress distributions for different locations on the cross-section of Fig. 2.

the action of the wind, is kept constant, varying the longitudinal pressure gradient to simulate the whole set of flow configurations that can be encountered in wind-induced 3D flows (see Fig. 3).

3. Formulation of the problem

Fig. 4 shows a sketch of the flow domain in which five possible shear stress distributions, resulting from different combinations of pressure gradient and plate velocity, are shown. Note that either plate can be moving, having chosen the high-stress plate as the origin for the y-axis.

To characterize the flows it is useful to introduce the parameter γ as in El Telbany and Reynolds [4], which represents the ratio of the shear stresses at the two walls

$$\gamma = \frac{\tau_2}{\tau_1} \tag{2}$$

where the subscripts 1 and 2 denotes the largest and smallest wall stress respectively.

Referring to the shear stress distributions of Fig. 4, pure Couette (a) and pure Poiseuille (e) flows are then characterized by values of γ equal to 1 and to -1, respectively and, scaling the shear stress with its maximum, the value of γ is always comprised between these values. All the c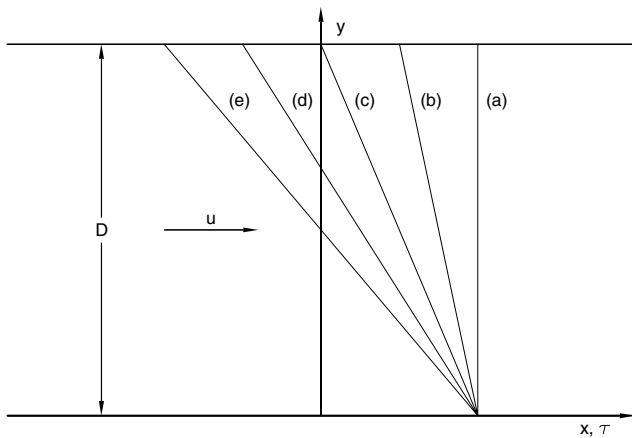onfigurations in which the shear stress remains positive, like in case (b), are associated with positive values of γ and are denoted as Couette-type (C) flows, while case (d) is representative of Poiseuille-type (P) flows ($\gamma < 0$), in which the shear stress distribution always changes sign along the vertical. Finally case (c) represents the configuration in which the shear stress at one wall is zero ($\gamma = 0$), a stress profile that resembles that of a conventional uniform flow in the absence of wind.

In the following, the notation F^+ indicates that the generic quantity F has been made nondimensional using the largest friction velocity u_{*1}, the molecular kinematic viscosity v and the fluid density ρ. The distance D between the plates appears then as the Reynolds number $Re = u_{*1}D/v$.

Under the above hypotheses the steady longitudinal momentum equation can be written as

$$\frac{\mathrm{d}}{\mathrm{d}y^+}\left[(1 + v_t^+)\frac{\mathrm{d}u^+}{\mathrm{d}y^+}\right] = -\frac{1 - \gamma}{Re} \tag{3}$$

where u^+ is the longitudinal velocity and v_t^+ is the eddy viscosity.

Eq. (3) has to be solved with boundary conditions of no-slip (or, equivalently, with the imposition of the shear stress) at the two walls and requires the specification of the y^+-dependence of the eddy viscosity v_t^+. Such vertical profile of the eddy viscosity is one of the expected outputs of the present analysis, so no guesses have been made on its structure and a two-equations turbulence closure, which will be outlined in the following, has been adopted for the solution. Note that (3) can be integrated once leading to

$$\frac{\mathrm{d}u^+}{\mathrm{d}y^+} = \frac{\tau^+}{1 + v_t^+} = \frac{1}{1 + v_t^+}\left[1 - \frac{y^+}{Re}(1 - \gamma)\right] \tag{4}$$

Although complex turbulence closures are not suitable for inclusion in Q3D models, they provide a considerable insight on the turbulence characteristics and have therefore been used to investigate wind-driven flow. Among others, countercurrent flow were investigated by means of a k–L one-equation model [11] or by the classical two-equation k–ε model [17].

Two-equation turbulence closures can be used to predict a given turbulent flow with no a priori information other than boundary conditions required in order to achieve a solution. In other words they do not require

Fig. 4. Sketch of coordinate system and possible shear stress distributions.

any guess on both the length and the velocity characteristic scales that locally describe the turbulence dynamics. Despite their apparent simplicity, however, C–P flows are a challenging test case for turbulence closures, since some features of these flows, namely the negative production of turbulent kinetic energy between the location of zero shear stress and the velocity maximum in P-flows or the situation of vanishing shear stress at a boundary, require particular care in modeling [6].

In particular, a word of caution should be spent on a standard application of the k–ε model. As it will be shown in Section 4, in fact, the equilibrium wall-layer in which production and dissipation of turbulent kinetic energy balance, disappears as the boundary shear stress tends to vanish. The conventional k–ε is very ill-behaved in this situation since the boundary condition on the dissipation rate ε becomes physically uncertain. Moreover, integration of k–ε transport equations is usually not performed up to the actual boundary but is instead stopped (or started) at some point inside the wall equilibrium layer. Modifications to the standard k–ε have been proposed [9] to allow for numerical integration throughout the viscous sublayer with the aid of viscous damping functions that, however, make the equations very stiff.

Since the present contribution is focussed on the determination of the behaviour of the turbulent characteristic scales in C–P flow more than on a detailed analysis on the local behaviour of the turbulent energy and dissipation balances, the k–ω model of Wilcox [22] has been chosen to investigate the eddy viscosity structure for turbulent Couette–Poiseuille flows. This model, which will be briefly summarized in the following, is based on two transport equations for the turbulent kinetic energy k and for the specific dissipation ω.

The eddy viscosity is assumed to be related to these two quantities by the relationship

$$v_t \propto \frac{k}{\omega} \qquad (5)$$

The model of Wilcox [22] is not subject to some of the above-mentioned shortcomings [21]. In particular, the model equations are valid inside the viscous sublayer with no need for artificial damping functions, thus allowing for integration through the viscous sublayer and for imposition of no-slip conditions at the walls. Moreover, the model is known to accurately predict the proper wake strength in equilibrium adverse pressure gradient boundary layers [12]. Finally, the value of the constants that appear in the model has been determined on the basis of theoretical arguments and therefore are assumed to be universal.

For turbulent Couette–Poiseuille flow the model equations can be written in dimensionless form as

$$\frac{\partial k^+}{\partial t^+} = (P_k - D_k)k^+ + \frac{\partial}{\partial y^+}\left[K_k \frac{\partial k^+}{\partial y^+}\right] \qquad (6)$$

$$\frac{\partial \omega^+}{\partial t^+} = (P_\omega - D_\omega)\omega^+ + \frac{\partial}{\partial y^+}\left[K_\omega \frac{\partial \omega^+}{\partial y^+}\right] \qquad (7)$$

where time t^+ plays the role of a relaxation parameter,

$$P_{(k,\omega)} = \frac{\alpha_{(k,\omega)}}{\omega^+}\left(\frac{\partial u^+}{\partial y^+}\right)^2 \qquad (8)$$

$$D_{(k,\omega)} = \beta_{(k,\omega)}\omega^+ \qquad (9)$$

$$K_{(k,\omega)} = (1 + \sigma_{(k,\omega)}v_t^+) \qquad (10)$$

and finally, the eddy viscosity is defined as the ratio

$$v_t^+ = \frac{k^+}{\omega^+} \qquad (11)$$

The constants appearing in the model have been chosen, according to Wilcox [22], as

$$\alpha_k = 1, \quad \beta_k = 9/100, \quad \sigma_k = 1/2, \qquad (12)$$

$$\alpha_\omega = 5/9, \quad \beta_\omega = 3/40, \quad \sigma_\omega = 1/2. \qquad (13)$$

Eqs. (3) and (6)–(11) form a closed set. Standard [22] boundary conditions are prescribed at each wall for k^+ and ω^+, namely

$$k^+ = 0 \quad \text{at } y^+ = 0, Re \qquad (14)$$

$$\omega^+ = \omega_w^+ \quad \text{at } y^+ = 0, Re \qquad (15)$$

where the value of ω_w^+ is specified as a function of the nondimensional roughness of the wall K_R^+

$$\omega_w^+ = \begin{cases} \left(\frac{50}{K_R^+}\right)^2 & \text{smooth } RK_R^+ < 25 \quad \text{(a)} \\ \frac{100}{K_R^+}R & \text{rough } RK_R^+ > 25 \quad \text{(b)} \end{cases} \qquad (16)$$

and the parameter R is equal to 1 for the high-stress plate and to $|\gamma|^{\frac{1}{2}}$ for the low-stress plate.

Finally, to improve numerical accuracy, a coordinate transformation of the kind

$$\eta = \frac{1}{2}\left[1 - \frac{\ln\left(\frac{a+1-y^+/Re}{a+y^+/Re}\right)}{\ln\left(\frac{a+1}{a}\right)}\right] \qquad 0 \leqslant \eta \leqslant 1 \qquad (17)$$

has been introduced that increases the number of node points close to the boundaries depending on the small parameter a.

4. Comparison with experimental data

In order to test the accuracy of the numerical predictions, a comparison with the experimental measurements of El Telbany and Reynolds [4] has been performed. The latter set of hot-wire time-mean velocity measurements represents the most extensive collection of data on turbulent C–P flows. The parameter γ of the experiments covers the whole range $-1 \leqslant \gamma \leqslant 1$.

Moreover, experimental distributions of the shear stress match quite well the linear law we are using as a starting point for our analysis of local equilibrium. Table 1 lists the leading features of the runs that were numerically simulated.

In Fig. 5 a comparison of the calculated velocity profiles with the experimental measurements is presented. Purposely, the same scalings that appear in the cited work have been adopted for these plots: velocities have been scaled with the belt velocity u_b (or with the maximum velocity for the Poiseuille flow); if the high-stress wall is fixed, u is the local fluid velocity while if it is moving, u is the relative velocity of the fluid.

The overall agreement for both P-type and C-type flows is quite good and the error can be quantified in a few percent.

As expected, C-type profiles have their maximum at the wall, while the plane of maximum velocity falls inside the flow domain for P-type flows. For the latter class of flows, the numerical solution, based on the Boussinnesq hypothesis, enforces the overlapping of the plane of maximum velocity and of the zero-stress plane, a condition which has been questioned based on experimental evidence [4] and on numerical prediction [6]. However, due the flatness of the velocity profile in this region, the differences in the location of the maxima lead to very small differences on the calculated versus predicted velocity profiles.

Fig. 6 shows a comparison of the calculated shear stress distributions with the experimental measurements. Again, the overall agreement is acceptable even though slight differences (less than 4% when scaled with the higher stress) were found in the calculated wall shear stresses with respect to the experimental values, ultimately leading to corresponding errors on the calculated value of γ. Note that once the flow velocities at the two walls and the slope of the shear stress distributions are fixed, the values of the shear stresses at the two walls re-
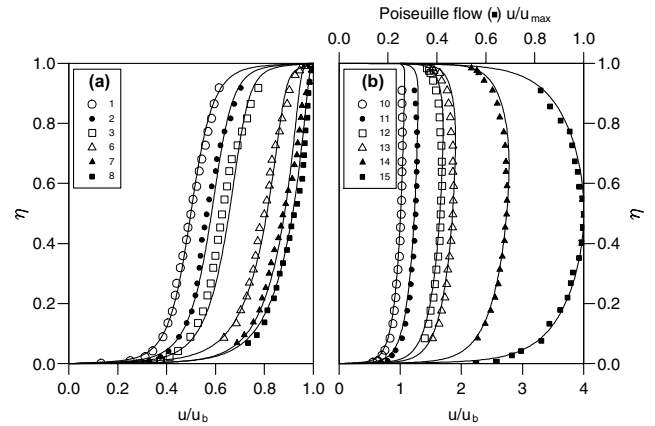

Fig. 5. Comparison of the calculated velocity profiles with the experimental data of El Telbany and Reynolds [4]. The corresponding Run numbers (see Table 1) are shown in the legends. (a) C-type flows and (b) P-type flows.
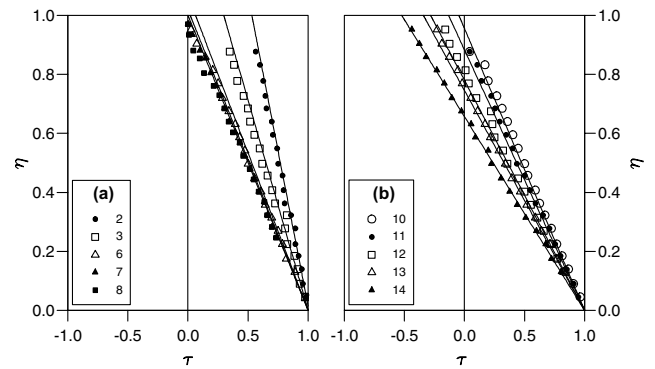

Fig. 6. Comparison of the calculated shear stress distributions with the experimental data of El Telbany and Reynolds [4]. The corresponding Run numbers (see Table 1) are shown in the legends. (a) C-type flows and (b) P-type flows.

sult from the integration of (3) and cannot be imposed a priori.

A good representation of both the velocity and the shear stress distributions implies, due to (4), a good representation of the eddy viscosity behaviour as a whole. Since the main purpose of the present contribution was to obtain suitable eddy viscosity profiles for wind-driven flows aiming at an algebraic interpretation of the latter, the overall agreement of the numerical results with the experimental values shown in Figs. 5 and 6 is satisfactory. Indeed, more interesting from the point of view of the physical interpretation of the results are the semi-logarithmic plotting of the velocity profiles in wall-coordinate presented in Figs. 7 and 8.

Fig. 7 shows the behaviour of the velocity profiles in the neighborhoods of the high-stress wall. A substantial collapse of both the numerical predictions and the measured data onto the logarithmic and viscous laws, shown as dashed lines, is found. The behaviour of the velocity close to the low-stress wall differs significantly from that
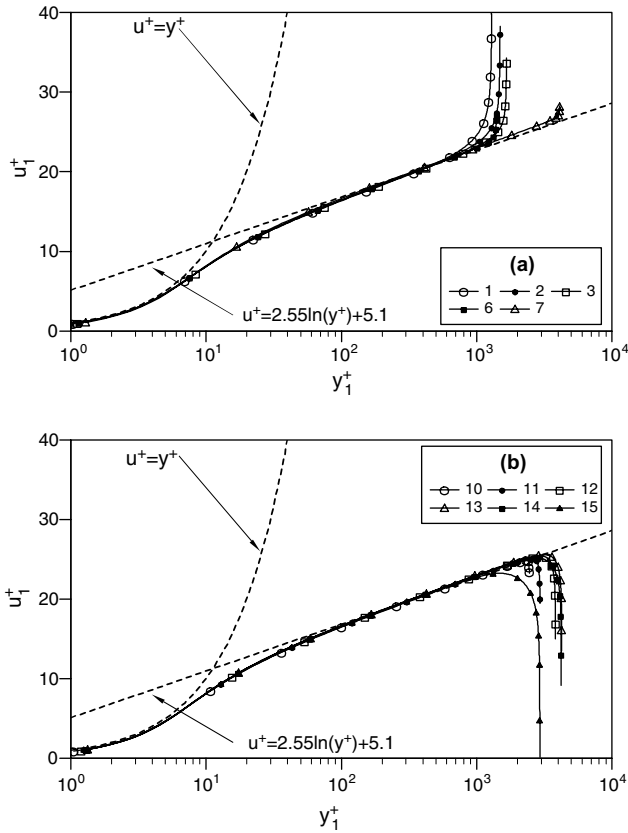
Table 1
Main parameters of some experimental runs of El Telbany and Reynolds [4] used for the comparison with numerical predictions

Run	D [mm]	U_b [ms^{-1}]	$Re = u_{*1}D/\nu$	u_{*1} [ms^{-1}]	u_{*2} [ms^{-1}]	$\gamma = u_{*2}/u_{*1}$
1	66	12.84	1257	0.282	0.282	1
2	66	12.84	1463	0.328	0.233	0.504
3	66	12.84	1614	0.362	0.1809	0.250
6	66	8.59	1396	0.313	0.0615	0.0386
7	101	17.08	–	0.6	0.04	0.0044
8	101	12.84	–	0.485	0.0229	0.00223
10	66	12.84	2515	0.504	0.03	−0.0028
11	66	12.84	3028	0.679	0.186	−0.075
12	66	12.84	3924	0.88	0.4142	−0.2215
13	66	12.84	4361	0.978	0.518	−0.2805
14	66	8.59	4285	0.961	0.67	−0.485
15	66	0	2938	0.659	0.659	−1

The original numeration of the experiments is retained.

Fig. 7. Semi-logarithmic plotting of velocity profiles at the high-stress wall. (a) C-type flows; (b) P-type flows. The friction velocity u_{*1} has been used for scaling both y_1^+ and u_1^+.
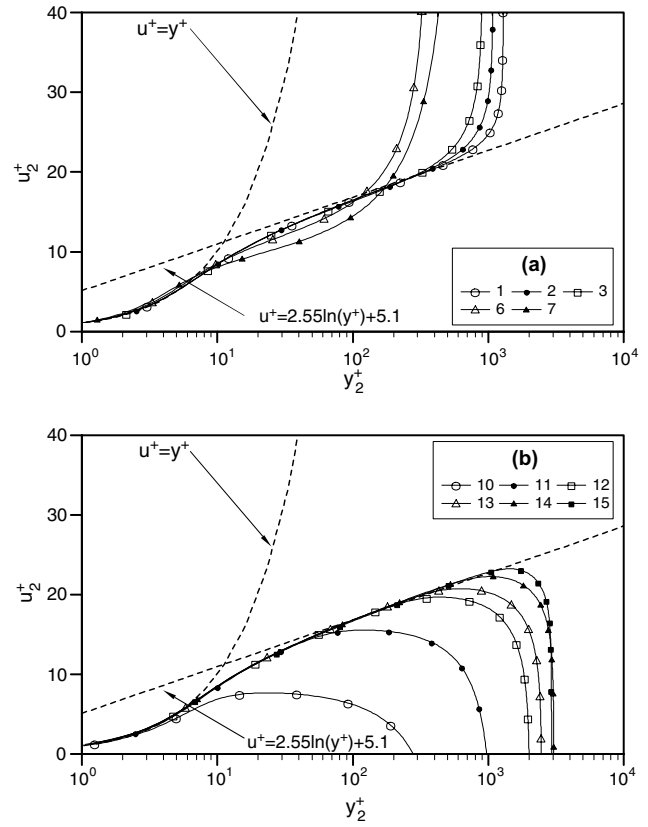

Fig. 8. Semi-logarithmic plotting of velocity profiles at the low-stress wall. (a) C-type flows; (b) P-type flows. The friction velocity u_{*2} has been used for scaling both y_2^+ and u_2^+.

at the other wall, as shown in Fig. 8. In the latter the friction velocity u_{*2} has been used to scale both y_2^+ and u_2^+.

For values of $|\gamma|$ of order 1 there is still a reasonable agreement with the line that represents the logarithmic law, while as γ tends to zero, the velocity profiles curve away. The point of departure from the logarithmic law moves toward the wall until, when $|\gamma|$ is sufficiently small, the viscous layer is reached and the logarithmic equilibrium layer no longer exists.

This behaviour, analyzed for the first time several years ago in some seminal studies of boundary layers in adverse pressure gradients [16,18], is typical of flow with negligible wall stress and is often referred to in boundary layer theory as the "erosion" of the logarithmic layer.

We postpone to the following section the discussion on the implications that this fact has on the turbulent processes (namely on the eddy viscosity structure) in the vicinity of the low-stress wall. The two plots of Fig. 9, showing the production and dissipation terms of the turbulent kinetic energy equation (6) in the vicinity of the walls, confirm the fading of the logarithmic layer for small values of the wall shear stress. The simulation is relative to a value of γ equal to 0.0044 (run 7) and shows that close to the high-stress wall a substantial
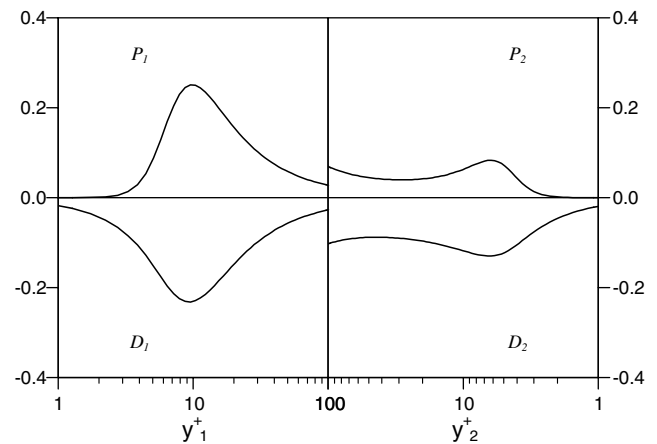

Fig. 9. Semi-logarithmic plot of the production ($P_{1,2}$) and dissipation ($D_{1,2}$) terms of the turbulent kinetic energy equation (6) in the vicinity of the high-stress (left) and of the low-stress (right) wall. The friction velocities u_{*1} and u_{*2} have been used for scaling in the left and right plot, respectively.

balance between the two terms occurs, while the opposite is true in the neighboring of the low-stress wall. Note that in this situation the use of "equilibrium" boundary conditions at the low-stress wall would be

inadequate and so predictions obtained with the conventional k–ε model would have been rather inaccurate.

5. Algebraic eddy viscosity distributions

The eddy viscosity distributions obtained by the numerical model have been analyzed in order to establish a suitable framework in which analytical profiles of eddy viscosity can be devised that account for the effect of wind. Indeed, the main goals of the present contribution are to show, firstly, that simple algebraic eddy viscosity models can successfully describe the vertical momentum exchange of wind-driven flows in shallow basins and secondly, that care must be used in the choice of the proper vertical distribution of the eddy viscosity in order to handle shallow flows driven by the concurring action of wind and tide.

This section is largely devoted to the analytical interpretation of the behaviour of the function $N(\eta, \gamma)$ defined as

$$v_t = u_{*1}DN(\eta, \gamma) \tag{18}$$

where u_{*1} is the maximum friction velocity, D is a characteristic vertical scale (either the distance between the plates or the local flow depth) and the origin of the vertical axis η has been set on the high-stress boundary. Hydraulically smooth conditions are assumed in (18), thus neglecting the role of boundary roughness.

Fig. 10 shows the calculated profiles of the function N for different values of γ. The simulations were made with a Reynolds number Re equal to 20 000. All the calculated profiles collapse onto an almost linear behaviour at the high-stress boundary, while sensible differences are detectable close to the low-stress boundary as γ varies. The kink present in P-type profiles is due to the presence of a zero-stress plane inside the domain, a feature
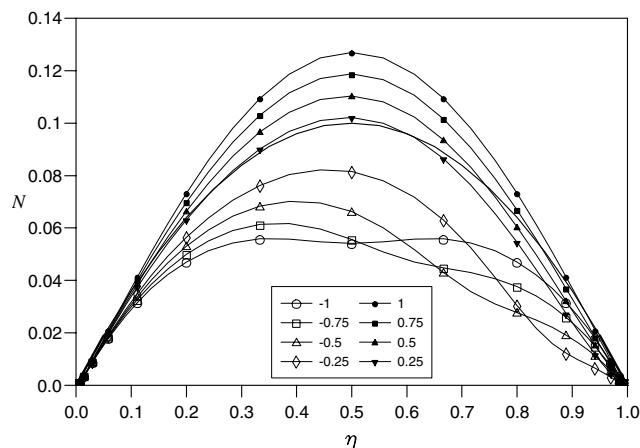
that is absent in C-type flows. The maximum value of N varies considerably with γ and is more than doubled moving from the pure Poiseuille to the pure Couette flow.

An obvious starting point for the analysis of algebraic profiles of eddy viscosity in free surface flows is the parabolic profile

$$N = \kappa\eta(1 - \eta) \tag{19}$$

that is shown for comparison in Fig. 10, having set the value of the von Kármán constant κ equal to 0.4. Even simpler model for which the eddy viscosity is constant [10] or, at most, constant in the core region and linear in a neighbourhood of one [13] or both [3,1] boundaries, are not considered herein.

No dependence on γ is present in (19), this resulting from the assumption that only one turbulent velocity scale enters the problem, in particular the wind friction velocity [19] or the maximum between the wind and the bottom friction velocities u_{*1} [8]. The dependence on γ displayed by the calculated profiles of Fig. 10 shows that for wind-driven flow at least two turbulent velocity scales appears simultaneously. It is then useful to define the parameter Γ, which is the nondimensional friction velocity at the low-stress boundary.

The cubic polynomial

$$N = \kappa[F(\Gamma)\eta + (1 - \eta)]\eta(1 - \eta) \tag{20}$$

is the simplest distribution that is consistent with a linear behaviour, with different slopes, at the boundaries. The above relationship can be formally derived assuming that the characteristic nondimensional turbulent velocity scale, i.e. the term between square brackets in (20), varies linearly between 1 at the high-stress boundary and a generic, for the moment, $F(\Gamma)$ at the low-stress boundary.

In Fig. 11 the function $F(\Gamma)$ obtained by a regression on the calculated eddy viscosity in a neighbourhood of the low-stress boundary is shown. The dashed line represents the function $F(\Gamma) = \Gamma$. Note that using Γ instead of $F(\Gamma)$ in (20), the cubic distribution originally proposed by Signell et al. [14] is recovered.

The results presented in Fig. 11 show that the nondimensional turbulent velocity scale F is equal to the local friction velocity Γ only for $\Gamma \sim O(1)$, while F is larger than Γ and tends to unity as $\Gamma \to 0$. These results are consistent with the considerations developed in the previous section based on the analysis of Figs. 7 and 8. In particular, at the low-stress wall it has been shown that: (i) a logarithmic layer exists for $\Gamma \sim O(1)$, characterized in term of the local friction velocity u_{*2}; (ii) as $\Gamma \to 0$, the logarithmic layer disappears.

Moreover, in the limiting case $\Gamma = 0$ presented in Fig. 12, the parabolic distribution (19) fits quite well the calculated one suggesting that only one characteristic turbulent velocity scale, namely u_{*1}, enters the problem.
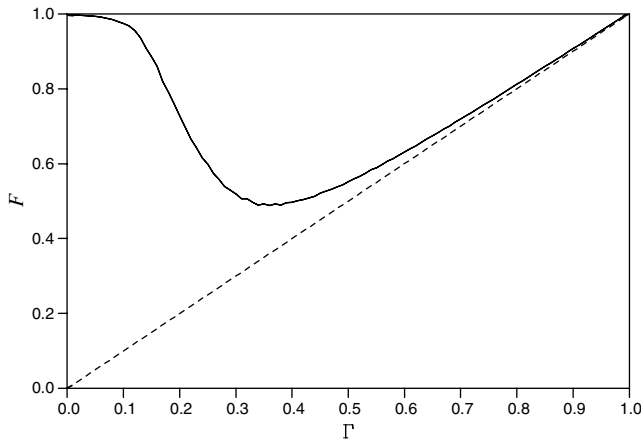

Fig. 10. Calculated profiles of the eddy viscosity function N for different values of γ as indicated in the legend. The thick solid line represents the parabolic profile (19).

Fig. 11. Calculated profile of the function F of (20) versus Γ. The dashed line is the function $F = \Gamma$.
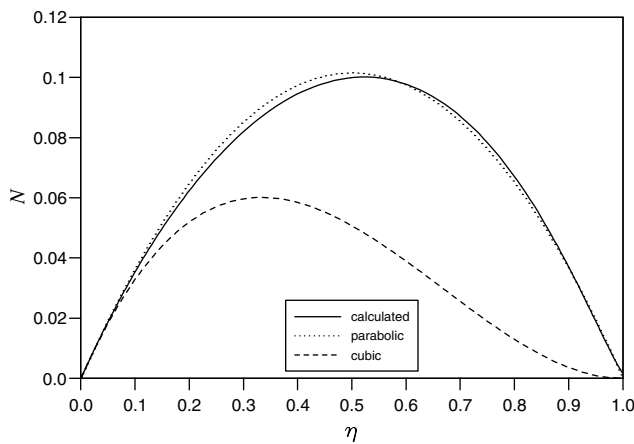

Fig. 12. Calculated profile of the eddy viscosity function N for the case $\Gamma = 0$. The corresponding cubic distribution of Signell et al. [14] and the parabolic function (19) are also shown.

In this case (20) reduces to the parabolic profile (19) since F is equal to unity. Besides, using the vanishing local friction velocity Γ instead of F would imply the vanishing of the derivative of N at the boundary, a condition that strongly influences the whole distribution as shown in the same figure.

It must be pointed out that the limiting case $\Gamma \to 0$ is not only representative of the peculiar situation in which the bottom stress vanishes but, most important, it controls the behaviour of the eddy viscosity for the case of vanishing wind stress or, more generally, when $u_{*s} \ll u_{*b}$. Therefore, a better description of this limiting case will possibly improve the performances of a Q3D model when wind and tide participate together in generating a circulation flow.

As formulated, the distribution (20) is identical for P-type and C-type flow characterized by the same value of Γ. Fig. 10 shows that this is not the case for the core region, while at the boundary the two symmetric (for

$\pm \gamma$) distributions actually merge into one except for the smallest values of Γ when the location of the zero-stress plane present in P-type flows only, interferes with the behaviour of the eddy viscosity in the vicinity of the low-stress boundary.

Even with the proposed modifications, a cubic polynomial is not able to represent some other features of the calculated profiles shown in Fig. 10, namely the differences between C-type and P-type flows in the core region. As mentioned before the latter effect is mainly due to the change of sign that the shear stress distribution experiences for P-type flows, which produces a kink in the eddy viscosity profile. Eventually, this results in an overall lowering of the intensity of the eddy viscosity for P-type flows.

In order to better handle the different behaviours displayed by P-type and C-type flows, a quartic polynomial of the kind

$$N = \kappa[F(\Gamma)\eta + (1 - \eta) + G(\gamma)\eta(1 - \eta)]\eta(1 - \eta) \qquad (21)$$

is proposed, where a dependence on γ is introduced through the function G to differentiate P-type from C-type flows.

The function G has been evaluated by means of a regression on the whole set of calculated data and its dependence on γ is shown in Fig. 13. This function, which controls the maximum of the eddy viscosity distribution, is approximately equal to unity for positive values of γ and decreases linearly to the value of -1.5 in the negative half-plane. The vanishing of G in a narrow neighbourhood of $\gamma = 0$ witnesses the recovering of a parabolic structure in this region.

Finally, the performances of the proposed distributions (20) and (21) are analyzed in term of the relationship between the vertically averaged velocity, the wind stress and the bottom stress. Once implemented in a Q3D model, in fact, the above eddy viscosity distributions and the corresponding velocity profiles constitute the basis for the evaluation of all the quantities that
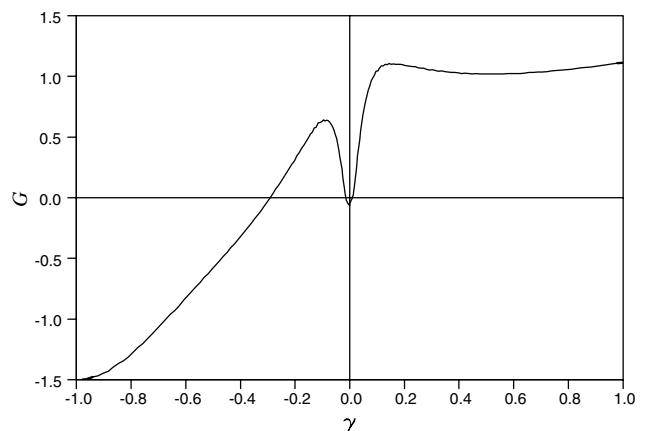

Fig. 13. Calculated profile of the functions G of (21) versus γ.

the primary shallow water flow solver requires in order to proceed in the calculation of the circulation flow, namely the bed shear stress and the depth-averaged dispersive stresses.

In Fig. 14, the bed to surface shear stress ratio is plotted versus the nondimensional depth-averaged velocity. Results obtained through the use of the quartic distribution (21) are almost undistinguishable from the calculated one, shown as a thicker solid line, and for this reason have not been plotted. This should indicate that the residual small errors related to the kinks present in P-type flows, which cannot be handled without further increasing the degree of the polynomial representing the eddy viscosity, have negligible influence on the bed shear stress evaluation.

The cubic distribution (20) still produces a fairly good agreement with the numerical results. The slight underestimation of the bed shear stress for positive values of the depth-averaged velocity is mainly due to the overall underestimation of the eddy viscosity in the core region for C-type flows. The introduction of the effective friction velocity F ultimately improves the performances of the model especially for vanishing γ, where the distribution proposed by Signell et al. [14] leads to a sharp underestimation of the bed shear stress.

The use a parabolic profile of the eddy viscosity with the assumption of the wind friction velocity u_{*s} being the only turbulent characteristic velocity scale, as suggested by Tsanis [19], leads to an unrealistic linear relationship between the bed shear stress and the depth-averaged velocity, as shown in Fig. 14. A careful choice of the constant of proportionality in (19), with a suggested value of 0.35 [19], conceals the weakness of this formulation for handling cases in which the bottom stress is larger (in modulus) than the wind stress. Increasingly high values of the average velocity yield values of the bed shear stress that are sharply underestimated with respect to the quadratic dependence, formally recovered in the case of negligible wind forcing, displayed by the numerical predictions and by all the profiles obtained by means of the cubic or quartic polynomials.

6. Conclusions

In the present contribution, the behaviour of the vertical profiles of eddy viscosity in uniform flows for different combinations of the shear stresses at the boundaries has been investigated, aiming at an improvement of the representation of the wind effect in the parametrization of turbulence.

Exploiting the analogy between wind-driven flows and turbulent Couette–Poiseuille flows, the latter have been analyzed by means of a two equation turbulent closure and a comparison with existing experimental data have been performed, showing an overall agreement between measured and calculated velocity profiles.

The calculated eddy viscosity distributions have been then analyzed and compared with currently available algebraic formulations, which were proposed to handle wind-driven flow, with specific attention on their behaviour in the mixed tide–wind case (or, more generally, when wind is not the only cause of motion). Two new algebraic formulations for the eddy viscosity are proposed, which are shown to improve turbulence description of this class of flows.

Further investigations will be required in order to estimate the role of bottom roughness, which can be included in the proposed formulations by a suitable shift in the origin of the reference level (i.e. the conventional
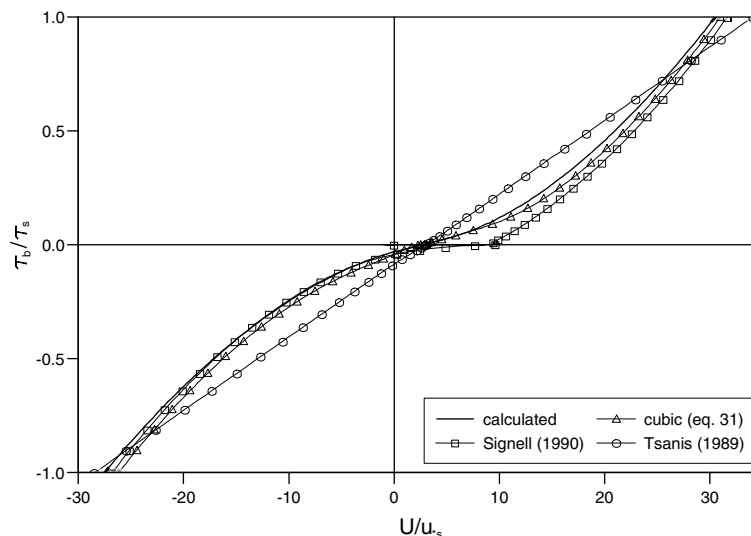

Fig. 14. Bed to surface shear stress ratio versus depth-averaged flow velocity for different formulations of the eddy viscosity.

level at which the logarithmic velocity vanishes) or, equivalently, by estimating the characteristic thickness of the wall layers.

References

[1] Al-Rabeh AH, Gunay N. On the application of a hydrodynamic model for a limited sea area. Coast Engng 1992;17:173–94.

[2] Baines WD, Knapp DJ. Wind driven water currents. J Hydraul Div ASCE 1965;91:205–21.

[3] Davies AM. On formulating a three-dimensional hydrodynamic sea model with arbitrary variation of vertical eddy viscosity. Comput Methods Appl Mech Engng 1980;22:187–211.

[4] El Telbany MMM, Reynolds AJ. Velocity distributions in plane turbulent channel flows. J Fluid Mech 1980;100:1–29.

[5] Falconer RA. Numerical modeling of tidal circulation in harbors. J Waterway Port Coast Ocean Div ASCE 1980;106:31–48.

[6] Gretler W, Meile W. Calculation of plane turbulent Couette–Poiseuille flows with a modified k–ε model. Fluid Dynam Res 1997;21:263–83.

[7] Goossens LT, van Pagee HJA, Tessel PJ. Vertical diffusion in air driven flows. J Hydraul Div ASCE 1982;108:995–1009.

[8] Jin X, Kranenburg C. Quasi-3D numerical modeling of shallow-water circulation. J Hydraul Engng ASCE 1993;119:458–72.

[9] Jones WP, Launder BE. The prediction of laminarization with a two-equation model of turbulence. Int J Heat Mass Transfer 1972;15:301–14.

[10] Koutitas C, Gousidou-Koutita M. A comparative study of three mathematical models for wind-generated circulation in coastal areas. Coast Engng 1986;10:127–38.

[11] Koutitas C, O'Connor B. Modeling three-dimensional wind-induced flows. J Hydraul Div ASCE 1980;106:1843–65.

[12] Menter FR. Influence of freestream values on k–ω turbulence model predictions. AIAA J 1992;30:1657–9.

[13] Pearce BR, Cooper CK. Numerical circulation model for wind-induced flow. J Hydraul Div ASCE 1981;107:285–302.

[14] Signell RT, Beardsley RC, Graber HC, Capotondi A. Effect of wave-current interactions on wind-driven circulation in narrow, shallow embayments. J Geophys Res 1990;95:9671–8.

[15] Simons TJ, Schertzer WM. Modelling wind-induced water set-up in Lake St. Clair. J Great Lakes 1989;15:452–64.

[16] Stratford BS. The prediction of separation of the turbulent boundary layer. J Fluid Mech 1959;5:17–35.

[17] Svensson U. Mathematical model of the seasonal thermocline. Rep No 1002, Dept Water Res Engng, University of Lund, Sweden, 1978.

[18] Townsend AA. The development of turbulent boundary layers with negligible wall stress. J Fluid Mech 1960;8:143–55.

[19] Tsanis IK. Simulation of wind-induced water currents. J Hydraul Engng ASCE 1989;115:1113–34.

[20] Tsanis IK, Leutheusser HJ. The structure of turbulent shear-induced countercurrent flow. J Fluid Mech 1988;180:531–52.

[21] Umlauf L. Turbulence parameterization in hydrobiological models for natural waters. PhD Dissertation, Technical University of Darmstadt, 2001.

[22] Wilcox DC. Turbulence modeling for CFD. La Cañada, California: DCW Industries; 1993.

[23] (a) Wu J, Tsanis IK. A vertical/horizontal integration wind-induced circulation model (VIH3D): a method for including surface and bottom logarithmic profiles. Adv Water Res 1995;18:77–87;
(b) Wu J, Tsanis IK. Numerical study of wind-induced water currents. J Hydraul Engng ASCE 1995;121:388–95.